



## Carnegie Airborne Observatory-2: Increasing science data dimensionality via high-fidelity multi-sensor fusion

Gregory P. Asner<sup>a,\*</sup>, David E. Knapp<sup>a</sup>, Joseph Boardman<sup>a,b</sup>, Robert O. Green<sup>c</sup>, Ty Kennedy-Bowdoin<sup>a</sup>, Michael Eastwood<sup>c</sup>, Roberta E. Martin<sup>a</sup>, Christopher Anderson<sup>a</sup>, Christopher B. Field<sup>a</sup>

<sup>a</sup> Department of Global Ecology, Carnegie Institution for Science, 260 Panama Street, Stanford, CA 94305, USA

<sup>b</sup> Analytical Imaging and Geophysics LLC, 4450 Arapahoe Avenue, Suite 100, Boulder, CO 80303, USA

<sup>c</sup> Jet Propulsion Laboratory, 4800 Oak Grove Drive, Pasadena, CA 91109, USA

### ARTICLE INFO

#### Article history:

Received 17 February 2012

Received in revised form 13 June 2012

Accepted 13 June 2012

Available online 4 July 2012

#### Keywords:

Airborne remote sensing

CAO

Data fusion

Hyperspectral

Imaging spectroscopy

LiDAR, Light detection and ranging

Macroscale ecology

### ABSTRACT

The Carnegie Airborne Observatory (CAO) was developed to address a need for macroscale measurements that reveal the structural, functional and organismic composition of Earth's ecosystems. In 2011, we completed and launched the CAO-2 next generation Airborne Taxonomic Mapping Systems (AToMS), which includes a high-fidelity *visible-to-shortwave infrared* (VSWIR) imaging spectrometer (380–2510 nm), dual-laser waveform *light detection and ranging* (LiDAR) scanner, and high spatial resolution *visible-to-near infrared* (VNIR) imaging spectrometer (365–1052 nm). Here, we describe how multiple data streams from these sensors can be fused using hardware and software co-alignment and processing techniques. With these data streams, we quantitatively demonstrate that precision data fusion greatly increases the dimensionality of the ecological information derived from remote sensing. We compare the data dimensionality of two contrasting scenes – a built environment at Stanford University and a lowland tropical forest in Amazonia. Principal components analysis revealed 336 dimensions (degrees of freedom) in the Stanford case, and 218 dimensions in the Amazon. The Amazon case presents what could be the highest level of remotely sensed data dimensionality ever reported for a forested ecosystem. Simulated misalignment of data streams reduced the effective information content by up to 48%, highlighting the critical role of achieving high precision when undertaking multi-sensor fusion. The instrumentation and methods described here are a pathfinder for future airborne applications undertaken by the National Ecological Observatory Network (NEON) and other organizations.

© 2012 Elsevier Inc. All rights reserved.

### 1. Introduction

Ecological research has trended toward questions of increasing complexity, particularly with respect to the interactions among organisms, including humans, with the environment at multiple spatial and temporal scales. This increasing complexity has come with the understanding that our biosphere is in a state of non-equilibrium change (Biggs et al., 2009). The velocity of climate change, and the pace of land-use change, now likely exceed the migration potential of many species and functional groups of species (Asner et al., 2010; Loarie et al., 2009), and this process has already begun to rearrange the composition of our biosphere (Parmesan, 2006; Wake et al., 2009).

With scientific questions increasingly focused on large-scale compositional change in our biosphere, the breadth and sophistication with which observations are made have rapidly evolved. There is much ongoing effort throughout the research community to advance observational capabilities in the field, in laboratories, and with

remote sensing. New field-based sensor networks are being designed to record changes in specific compositional properties and their controls, such as animal presence and ambient temperatures, distributed over space and time (Porter et al., 2005). In the lab, advances in high-throughput genetic and chemometric assays have increased our ability to observe patterns of compositional change among samples collected throughout ecosystems (Ratnasingham & Hebert, 2007). And space-based observing has increased our ability to detect global-scale changes in forest cover, regional variation in community type, and sub-regional patterns of plant functional type or target species (Turner et al., 2003).

Satellite technology is powerful because it provides vegetation metrics over large regions – metrics which integrate multiple ecological properties and processes into a single measurement. For example, the normalized difference vegetation index (NDVI) – a metric of canopy greenness (Hatfield, 1984) – integrates variation in leaf chemical properties, leaf area index, canopy architecture, species composition, land cover and other factors (DeFries & Townsend, 1995; Gitelson & Merzlyak, 1997; Sellers, 1985; Verma et al., 1993). As a result, the NDVI has been used in many studies linking greenness to integrated plant performance variables such as primary productivity (e.g., Field

\* Corresponding author. Tel.: +1 650 462 1047.

E-mail address: [gpa@stanford.edu](mailto:gpa@stanford.edu) (G.P. Asner).

et al., 1998). However, macroscale ecology has evolved to recognize the separate roles that vegetation structure, function, and organisms play in regulating carbon and water cycles, biological diversity and other biospheric properties and processes (Bonan et al., 2002; Medvigy et al., 2009). Traditional satellite metrics may be correlated with these factors, but rarely so in a way that provides quantitative attribution to specific drivers of change. As a result, there remains a need for macroscale observations that reveal differential changes in vegetation structure, function and composition. Spatially-explicit observations could also help the remote sensing and modeling communities to incorporate an enormous amount of field-based data available on myriad vegetation properties. For this, the airborne perspective has proven extremely powerful.

Airborne observation is one of the oldest forms of remote sensing (Fensham & Fairfax, 2002), and the technology has advanced from monochromatic analog cameras to high-fidelity spectral-optical, radar, and LiDAR (light detection and ranging) technologies. Contemporary studies using modern airborne sensors have typically focused on a specific observation, such as vegetation type from optical cameras, canopy height from LiDAR and radar, or canopy chemistry from spectrometers (Lefsky et al., 2002; McGraw et al., 1998; Ustin et al., 2004). More recently, efforts to combine data from different technologies, often collected from separate aircraft, have yielded multi-dimensional data that more closely address emerging scientific questions on changing biospheric composition (Clark et al., 2011; Medvigy & Moorcroft, 2012; Thomas et al., 2006; Varga & Asner, 2008). These and other studies have provided justification for the use of multi-sensor observations to increase data dimensionality.

In this context, the Carnegie Airborne Observatory (CAO) was developed to more fully probe the structure, function and composition of ecosystems at the macroscale of thousands to millions of hectares. In 2006, a *visible-to-near infrared* (VNIR) imaging spectrometer and waveform LiDAR scanner were integrated into a system called CAO-Alpha (Asner et al., 2007). The premise behind the CAO, starting with the Alpha system and continuing up to the present, is that a fully integrated set of orthogonally-distributed observations, incorporating measurements expressly selected for multi-dimensional analysis of ecosystems, would advance our understanding of the biosphere in three ways: (i) by resolving ecological properties at scales commensurate with the flows of energy, materials, and organisms (gene flow) within and among ecosystems; (ii) by developing new understanding at the macroscale, yet with fine biological resolution, that

is largely intractable from the orbital vantage point; and (iii) by facilitating fundamental discoveries that have eluded ecology in the past. As of June 2012, the CAO has supported more than 100 collaborator-led studies and dozens of internal projects, with ecological results reported in more than 70 peer-reviewed papers reflective of progress in each of these three areas (<http://cao.ciw.edu>). However, studies in the CAO-Alpha era also highlighted a need to further increase the dimensionality of the airborne data, particularly in terms of vegetation function (chemistry) and biological diversity. Following a concurrent activity to define technology and science-algorithm requirements, the next generation CAO-2 Airborne Taxonomic Mapping System (AToMS) was launched in June 2011.

Here we introduce CAO-2 AToMS, providing details on its specifications and performance levels. We then quantitatively analyze how fusing instruments and their data streams increases the dimensionality of the ecological information derived from remote sensing. The term *data fusion* refers to the combining of sensory data from disparate sources such that the result expresses more information than is possible when the data sources are used individually. We also use the term *co-alignment* to indicate a subset of the data fusion processes involving aligning of image pixels and LiDAR laser spots. Overall, the instrumentation and methods presented here serve as a pathfinder for macroscale ecological applications undertaken by other organizations. In particular, results and techniques derived by the CAO program support the goals and plans of National Ecological Observatory Network (NEON) and other agencies (Kampe et al., 2011).

## 2. CAO-2 AToMS

AToMS is comprised of three major sensors and their associated onboard control and computing systems: (i) *visible-to-shortwave infrared* (VSWIR) imaging spectrometer; (ii) waveform LiDAR; and (iii) *visible-to-near infrared* (VNIR) imaging spectrometer (Fig. 1). The VSWIR provides full-range (380–2510 nm) spectroscopic radiance measurements with very high fidelity needed for canopy chemical and physiological applications, as well as for geological and atmospheric measurements. The LiDAR provides detailed three-dimensional (3-D) data on vegetation structure, sub-canopy ground surface elevation, and the 3-D structure of non-vegetated targets. The VNIR spectrometer provides increased spatial detail, with 4 pixels per VSWIR pixel, covering the 365–1052 nm range. High spatial resolution is often needed to discern individual lifeforms and species.

The three instruments are aligned on a single reinforced steel plate which floats on six hi-damp silicon pneumatic mounts for vibration dampening (Fig. 1). The mounts are not designed for active stabilization control, but rather for providing a semi-rigid connection between the instrument sensor heads and aircraft, while minimizing vibration. The entire payload has a mass of approximately 850 kg.

### 2.1. VSWIR details

The VSWIR imaging spectrometer is a pushbroom linear array based on the Offner spectrograph design (Prieto-Blanco et al., 2006), and it is the cornerstone sensor within AToMS (Fig. 2). The CAO VSWIR measures upwelling spectral radiance in 5-nm increments (full-width at half-maximum) or 428 contiguous spectral bands (Table 1). Because very high spatial and spectral uniformity is required to produce high-fidelity spectrometer data (Green, 1998; Mouroulis et al., 2000), the VSWIR was designed and tested to ensure greater than 95% cross-track spatial uniformity and spectral IFOV uniformity at all wavelengths. Thermal control of the VSWIR vacuum chamber is critical to achieving the high levels of uniformity described. To manage this, we utilize temperature controllers with Si diode sensors at multiple control points within the thermal vacuum enclosure. Temperatures are held to within 0.1°K at all points for an

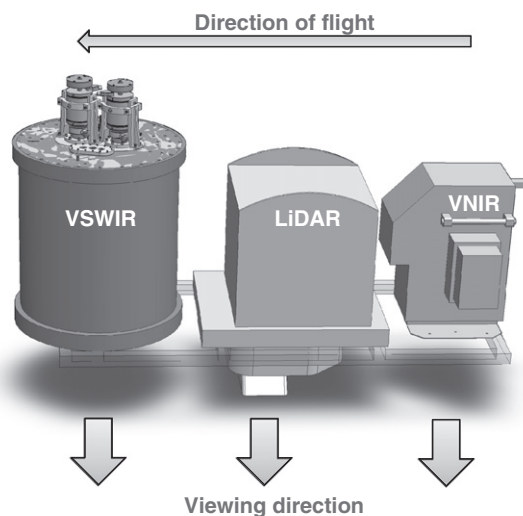


**Fig. 1.** Schematic view of the CAO AToMS sensor heads including, from left to right: visible-to-shortwave infrared imaging spectrometer (VSWIR), waveform light detection and ranging (LiDAR) scanner, and visible-to-near infrared imaging spectrometer (VNIR).

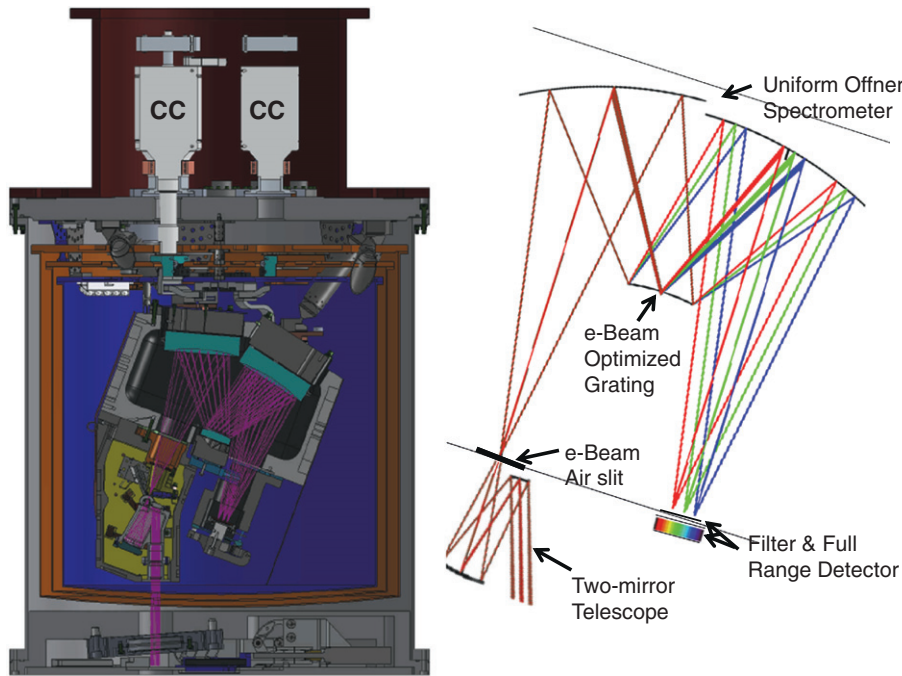


**Fig. 2.** Schematic of the cornerstone CAO instrument – the VSWIR spectrometer – showing the spectrometer body suspended by isolating struts in a thermally-regulated vacuum chamber. The ray trace for incoming light is shown on the left in purple color, with a more detailed view on the right. The two devices at the top of the VSWIR instrument are electric cryocoolers (CC).

external environment temperature range of 0–45 °C, providing optical alignment to within 2% of a spectral band.

The signal-to-noise (SNR) performance of the VSWIR is shown in Fig. 3. The reported SNR for the VSWIR benchmark radiances is derived from measured laboratory signal and noise values from the completed instrument. The CAO instrument is held in a vacuum vessel at cryogenic temperatures to isolate the spectrometer from pressure and temperature disturbances. With a 25% Lambertian reflectance target at 23.5° illumination zenith angle and a 0.01 s integration time, the VSWIR delivers arguably the highest performance levels reported for an operational full-range imaging spectrometer. For example, VSWIR SNR levels are two times higher in the visible (400–700 nm) range than its predecessor Airborne Visible and Infrared Imaging Spectrometer (AVIRIS). Moreover, VSWIR SNR is 300–500% higher than AVIRIS in the shortwave-infrared (1300–2510 nm), depending upon wavelength (see Green et al., 1998). The extremely high SNR and uniformity is required to meet CAO goals of mapping vegetation canopy chemistry, physiology and composition (Asner et al., 2007, 2011). In particular, it is important for resolving atmospheric water vapor and aerosol in the spectrum, so that these and other constituents can be modeled and accounted for while deriving apparent surface reflectance upon which vegetation and ecosystem mapping analyses depend (Green, 1998; Green et al., 1998, 2005).

Pushbroom spectrometers, particularly full-range instruments, are notorious for spectral and spatial non-uniformity across the detector array (Mouroulis & Green, 2003). To reach the high levels of uniformity required for macroscale ecological applications, we integrated an *on-board calibrator* (OBC) into the VSWIR spectrometer to allow ultra-fine tuning of the image radiometric calibration during flight. The OBC is a highly stable, feedback-controlled, color-balanced halogen lamp in a parabolic reflector providing a collimated beam into an off-axis parabolic mirror, which focuses the light down to a tight bundle. When a shutter in the focused beam is opened, light is transmitted into a fiber optic bundle comprised of approximately 350 low-OH 200  $\mu\text{m}$  fibers, which conducts the light from the OBC source module outside the thermal-vacuum enclosure through a hermetically

sealed portion of the fiber length, then through the inner thermal shields and down to a highly reflective target immediately in front of the spectrometer slit. The target has highly repeatable positioning and is coated with space-grade white paint that has no absorption features over the 380–2510 nm spectral range. This paint, APTEK Laboratories 95395, has aluminum oxide powder as pigment in a KASIL 2135 potassium silicate binder formulated specifically for higher reflectance in the blue end of the spectrum compared to other inorganic white paints. The actuated painted target in front of the spectrometer slit is illuminated by the OBC light immediately following the collection of each data flight line. This allows measurement of and compensation for any small changes in the spectrometer light response across the spectrum and across the full 34° field-of-view of the sensor. Stability has been demonstrated in the lab at the 0.1% level (Coles et al., 2011). The OBC fiber optic bundle also includes three fibers that allow a helium–neon laser to send 532.8 nm light onto the white target in front of the slit to confirm the spectral calibration of the spectrometer.

## 2.2. LiDAR details

The CAO-2 LiDAR is a dual-laser scanning system operating at 1064 nm (Table 1, Fig. 1). The LiDAR collects the full waveform and up to four discrete returns per laser shot. The effective pulse repetition rate is adjustable from 100 to 400 kHz in increments of 100. The scan frequency and angle can be adjusted independently to achieve desired spot spacing with maximums of 140 Hz and 65°, respectively. The waveform amplitude data are digitized at 8-bit and discrete return intensity data are digitized with 12-bit dynamic range. Laser beam divergences are 0.5 mrad (1/e) resulting in a 50 cm footprint at 1000 m above ground level (AGL). Horizontal accuracy is a function of height (Table 1), with a one-sigma uncertainty of 18 cm at 1000 m AGL. The elevation uncertainty is less than 15 cm at one-sigma.

## 2.3. VNIR details

The VNIR imaging spectrometer is based on the CASI-1500 design (Babey & Anger, 1989) with major customizations for higher data

**Table 1**

CAO ATOMS performance specifications including its visible-to-shortwave infrared (VSWIR) and visible-to-near infrared (VNIR) imaging spectrometers, and waveform light detection and ranging (LiDAR) scanner.

Component	Description
VSWIR	Type: pushbroom array, diffraction grating, Offner design Detector: HgCdTe Spectral range: 380–2510 nm Spectral resolution: 5 nm Spatial pixels: 600; 34° field-of-view Instantaneous field-of-view: 1.0 mrad 14-bit dynamic range Min. to max. radiance level: 0.0–70.0 mW cm <sup>-2</sup> nm <sup>-1</sup> sr <sup>-1</sup> Radiometric stability ≤2% Spatial uniformity: 95% Spectral uniformity: 97% SNR: see Fig. 3
LiDAR	Dual laser: one at nadir and one at 2.4° forward of nadir Wavelength = 1064 nm Full waveform digitization, 1 ns resolution Pulse repetition rate: 400 kHz max. Scan frequency: 140 Hz max. Scan angle: 65° max. 12-bit dynamic range Beam divergence: 0.5 mrad (1/e) Horizontal accuracy: 1/5500 × altitude (1 sigma) Elevation uncertainty: <15 cm (1 sigma)
VNIR	Type: pushbroom array, diffraction grating, Offner design Detector: Si Spectral range: 365–1052 nm Spectral resolution: adjustable 2.4 nm to 19.2 nm in 2.4 nm increments Spatial pixels: 1480; 40° field-of-view Instantaneous field-of-view: 0.5 mrad 14-bit dynamic range Min. to max. radiance level: 0.0–60.0 mW cm <sup>-2</sup> nm <sup>-1</sup> sr <sup>-1</sup> Radiometric stability ≤2% Spatial uniformity: 96% Spectral uniformity: 94% SNR at nadir = 410 @ 550 nm on 25% reflectance target SNR at nadir = 830 @ 850 nm on 25% reflectance target Downwelling irradiance sensor (350–2500 nm; 2.0 nm sampling) 200 Hz high-performance FOG gyros; silicon accelerometers
IMU	Performance: velocity = 0.005 m/s; roll and pitch = 0.005°; heading = 0.008°
GNSS	L1/L2 compatible; 43 dB 72 channel dual frequency; 20 Hz raw data rate
Sensor mount	Floating-plate design with six hi-damp Si pneumatic mounts for vibration dampening
Pilot controls	Navigation display controlled by instrument operator from rear of aircraft

rate, stability and signal-to-noise performance. The system has 1480 track-track elements spanning a 40° field-of-view (Table 1, Fig. 1). The instantaneous FOV is 0.5 mrad. The derived spectra have an adjustable number of spectral bands of up to 288 for a fixed wavelength range of 365–1052 nm. The VNIR readout provides ultra-fast data rates of up to 330 frames s<sup>-1</sup>. Anti-reflective coatings and a detector cooling sub-system result in SNR levels of up to 1800 in the near-infrared spectrum on a 25% reflectance target and 0.01 s integration time.

### 3. Instrument and data fusion

ATOMS is designed to serve a multi-dimensional data collection, processing and modeling stream (Fig. 4). Data from each instrument are integrated using a combination of hardware- and software-based fusion techniques. The co-alignment of the CAO data relies on the known relative position and orientation of the sensors within the aircraft. Sensor positioning information is acquired via post-processed differential correction between an airborne 220 channel Global Navigation Satellite System (GNSS) and ground based reference stations. Sensor orientation is measured with an *inertial measurement*

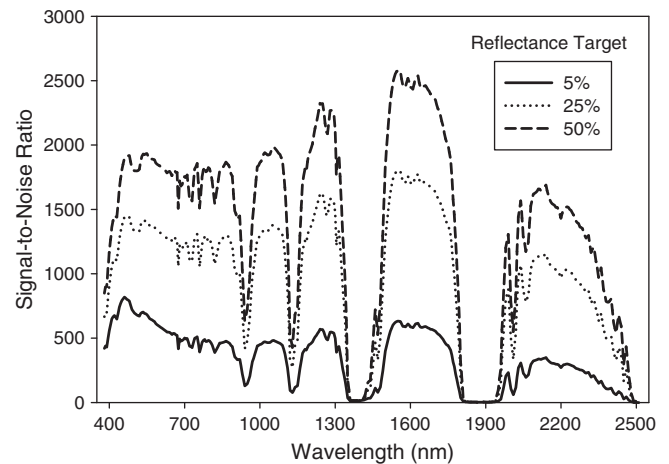


**Fig. 3.** Spectral signal-to-noise performance of the CAO VSWIR spectrometer at three different target reflectance levels: 5% (45° illumination zenith angle), 25% (23.5°), and 50% (23.5°). The results are based on a 0.01 s integration time using a laboratory calibration illumination source. For reference, the SNR is up to five times higher in the CAO VSWIR than in the Airborne Visible and Near-infrared Imaging Spectrometer (AVIRIS; Green et al., 1998).

unit (IMU) collecting three dimensional angular accelerations at 200 Hz. The position and orientation of each sensor is calculated at each frame step using a tightly coupled model combining GNSS and acceleration data to produce a *smooth best estimate of trajectory* (SBET) with accuracies better than 10 cm and 0.008°. The two spectrometers utilize the same SBET as the LiDAR to determine the location of every pixel in each image. To locate each pixel, the spectrometers and LiDAR must be synchronized with the times in the SBET. This is accomplished by reading a pulse-per-second signal from the GNSS, which is then time-stamped to each frame in the image data streams from both spectrometers.

To derive the most precise instrument fusion possible, it is necessary to create a three-dimensional camera model for each spectrometer. Each camera model takes into account the optical properties of the lens through which the light travels, the location of the pupil of the lens relative to the SBET referenced location, as well as small angular offsets due to slight differences in mounting the spectrometers. The field data needed to create the camera models include a series of known locations (map coordinates and pixel/line coordinates) of features observed in the LiDAR and spectral data (Fig. 5). Traditionally, this is accomplished by manually selecting ground control points and tie points (pixel/line coordinates) between various flight lines. However, because the LiDAR data are already very precisely geolocated by the SBET solution, the intensity data from the LiDAR points is used to produce an image at the wavelength of the laser (1064 nm), which can then be precisely matched to the same wavelength image in the spectrometers (Bay et al., 2008) (Fig. 6). Using coordinates of the correlated features found in all three data sets, the camera model parameters are computed to produce a precise final fit between data streams ( $\ll 1$  pixel RMSE).

We achieve both high accuracy and high precision in the co-registration and ray tracing process by employing a cross-sensor optimization scheme that uses spectrometer tie points and spectrometer-to-LiDAR-intensity virtual control points. Leveraging its spatial high accuracy and self-consistency, we modify the LiDAR intensity images to mimic a passive reflectance image by imposing shading and cast shadows. Automatic control points are generated to match image features in the LiDAR intensity and spectrometer imagery. Likewise we generate automatic tie points that link the significant overlap of spectrometer flight lines. We typically produce tens of thousands of these tie and control points per camera calibration experiment, and the points are divided up to provide calibration and independent validation.

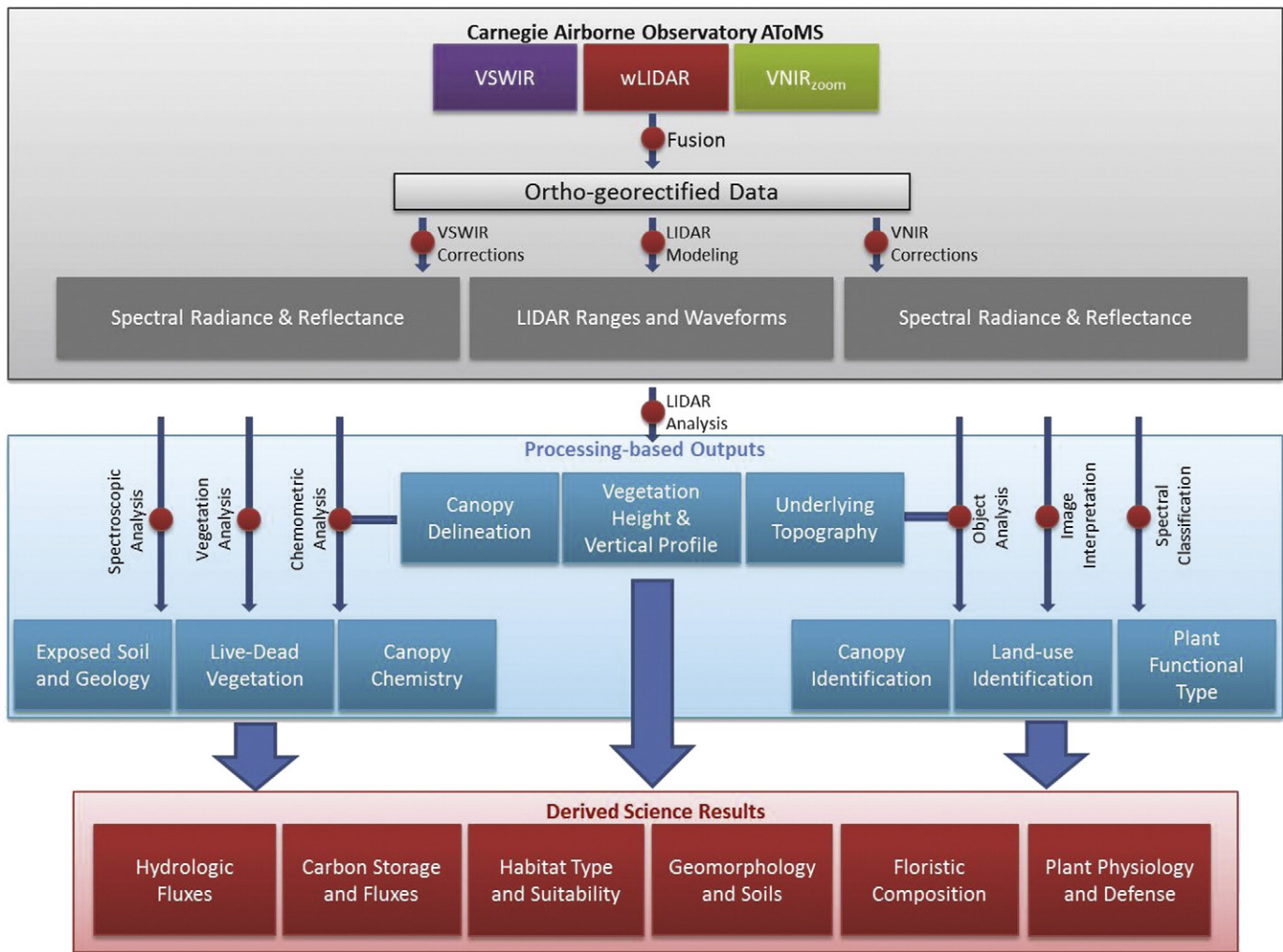


**Fig. 4.** Multi-dimensional information flow from raw data collected onboard the CAO (top section), to processed science data outputs (middle section), to scientific results derived through analysis and modeling.

By designing the calibration flight lines to have crossing fields-of-view, from different altitudes and different flight directions, we solve the model to optimize the absolute accuracy of the result by separating the effects of correlated variables such as pitch and timing, and field of view and altitude. The spectrometer camera calibrations are an eleven parameter model that accommodates the curved projection of the spectrometer slits and the sensor-to-body angles between the navigation frame and the optical axes of each instrument. We have shown that this self-calibration procedure is very sensitive and a good result virtually guarantees both accuracy and precision in the final camera models and resulting pixel locations. By combining all the data, we have developed an approach that is self-calibrating and self-validating for regions areas with overlapping flight lines. Any off-nominal performance, by the LiDAR or the spectrometers is revealed in the form of a failure of the model to converge to an acceptable residual.

#### 4. Science data flow

Following data fusion, which can result in 504–1204 bands of raw data depending upon VNIR and waveform LiDAR settings, the measurements are analyzed to science results using a variety of techniques (Fig. 4). Our purpose here is to briefly highlight the analytical options made available through high-fidelity measurements with precision data fusion, and to provide related references. First, high-fidelity spectroscopic data allow for quantitative atmospheric correction of the

spectra (Gao et al., 1993; Reinersman & Carder, 1995; Roberts et al., 1997): By combining high-SNR, contiguous narrowband spectra with precise geometric information from the SBET data, we develop reflectance spectra that minimize effects of aerosol, water vapor, and other atmospheric constituents (Gao & Goetz, 1990; Green & Pavri, 2002; Green et al., 1998, 2005; Schlaepfer et al., 1996). Second, automated and semi-automated techniques can be applied to spectroscopic data to derive a wide variety of ecological and geophysical properties (blue box, Fig. 4). Examples include chemometric analyses for soil and rock mineralogy (Clark et al., 2003; Swayze et al., 2000), spectral unmixing and classification of vegetation cover, live and dead material, functional types, and composition (Asner & Lobell, 2000; Bohlman, 2008; Clark et al., 2005; Kalacska et al., 2007; Roberts et al., 1998; Somers et al., 2011), and retrievals of canopy chemicals including photosynthetic pigments, nutrients and defense compounds (e.g., Knox et al., 2011; Kokaly et al., 2009; Martin et al., 2008; Ustin et al., 2009). In parallel to spectral analyses, LiDAR can be used to map vegetation biomass from the three-dimensional data provided on canopy height and structure (Harding et al., 2001; Lefsky et al., 2002; Mascaro et al., 2011). LiDAR data can also be used to model topography and to identify tree crowns and other objects in the imagery (Clark et al., 2004; Lee & Lucas, 2007; Müller & Brandl, 2009).

With an integrated use of LiDAR and spectral measurements, the interpretation of both data types can be greatly improved (Dalponte et al., 2008; Mundt et al., 2006), thereby enhancing multi-dimensional analyses of ecosystems. For example, biological diversity is detectable down

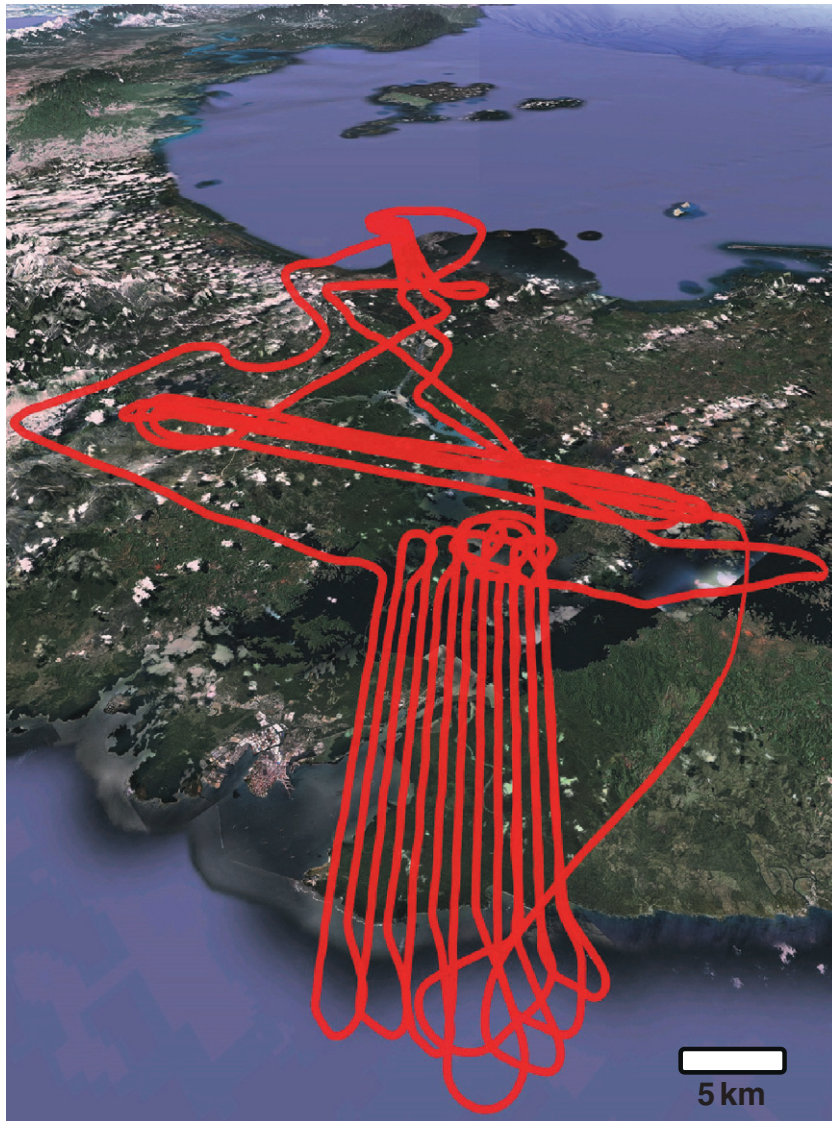


**Fig. 5.** A typical smoothed best estimate of trajectory (SBET) for a CAO mapping flight over the Republic of Panamá in January 2012. The precise location (latitude, longitude, and altitude) and orientation (roll, pitch, and yaw) of the focal points in each ATOMS sensor is displayed as a continuous red line. Lines appearing close together indicate areas of intensive mapping activity.

to organismic levels using a combination of spectral and LiDAR measurements that express the functional and structural traits of lifeforms and species (Asner et al., 2008; Blackburn, 2002; Hill & Thomson, 2005; Mundt et al., 2006; Ustin & Gamon, 2010). Vegetation habitat,

upon which the entire web of life depends, can be more deeply probed with fused spectral and LiDAR observations that express spatial variation in functional and structural plant characteristics (Boelman et al., 2007; Clark et al., 2011). By combining spectroscopically-derived

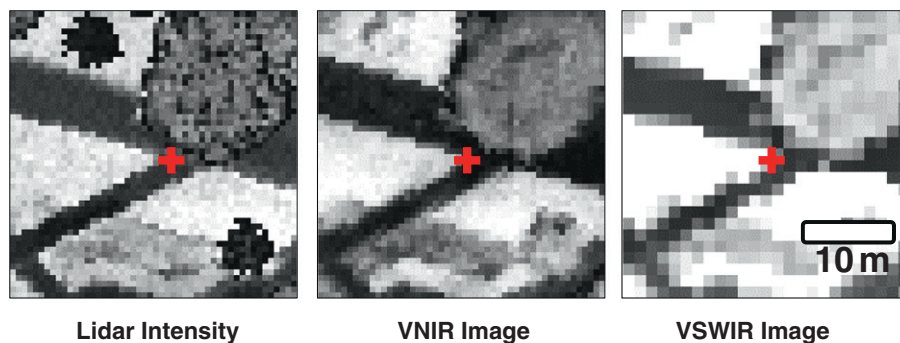


**Fig. 6.** A single point example from the CAO automated, inter-instrument tie-point selection algorithm, which produces thousands of tie-points to solve for geometric offsets in three dimensions. All images are tied at 1064 nm. This approach yields camera parameters for the VSWIR and VNIR spectrometers, resulting in digitally bore-site aligned geo-orthorectified imagery fused with the LiDAR-derived surface digital elevation model.

vegetation traits to estimate plant physiological processes (Doughty et al., 2011; Gamon et al., 1992), along with topography and structure from LiDAR observations, it is possible to develop spatially explicit information on hydrological flow and water quality (French, 2003). As demonstrated in the examples above, the science community is beginning to use these integrated measurement approaches, and the demand for the multi-dimensional information will continue to increase.

## 5. Science data dimensionality

The potential value of combining high-fidelity spectrometer and LiDAR measurements needs to be considered with respect to the potential gain in data dimensionality. The inherent dimensionality of fused data streams is dependent upon the orthogonality (or uniqueness) of the measurements, their noise levels, the accuracy of data co-alignment, and the composition of the imaged landscape. Here we use the fully integrated ATOMS data stream – including VSWIR, LiDAR and VNIR sensors – to assess the inherent data dimensionality of two contrasting environments (Fig. 7). One example data set of about 100 ha was collected in June 2011 over Stanford University in California USA, which is comprised of a mosaic of vegetation types (grasses, shrubs, trees, and palms), buildings with an array roofing materials, pavements, and exposed soils. Another 300 ha example was collected in July 2011 over a lowland humid tropical forest at the Los Amigos conservation concession in the Peruvian Amazon; it is comprised of a high diversity of tree, liana and other plant species (Phillips et al., 2009). The data sets are each comprised of VSWIR spectral reflectance signatures in 5-nm increments from 380 to 2510 nm, LiDAR data processed to vegetation height, topography, and vertical canopy profiles (see Asner et al., 2007), and VNIR spectral reflectance data in 10-nm increments from 370 to 1050 nm. The data were processed to match the ground sampling distance of the VSWIR sensor for each data set: 1 m for Stanford and 2 m for the Peruvian Amazon.

Principal components analysis (PCA) was used to estimate the dimensionality of the Stanford and Amazon data sets (Fig. 8). PCA converts a group of potentially correlated observations into a set of uncorrelated variables, or PCs. The first PC accounts for as much of the variability in the data set as possible, and each subsequent PC, in turn, captures the greatest variance possible under the constraint that it be orthogonal or uncorrelated with the preceding PCs. With remotely sensed imagery, it remains a challenge to quantitatively assess the number of significant PCs within a data set. Most practitioners compute a PCA, and then manually review each resulting PC band to seek recognizable spatial information, thereby discarding bands comprised of or dominated by noise. Here we manually reviewed the results of PCA using different combinations of measurements (VSWIR, LiDAR, and VNIR), with the criterion being that any PC band with features recognizable in the original imagery (e.g., buildings, tree crowns) would be counted as an additional degree of freedom in the data set. PC bands dominated by random noise were excluded from the count (Fig. 8). Although this approach may introduce some user bias, we limit our interpretation of it as a relative index comparing different sensor combinations.

With only the LiDAR data, there are 33 and 62 significant PCs, or spatial degrees of freedom, in the Stanford and Amazon cases, respectively (Fig. 9). By close inspection of the LiDAR data, we determined that the boosted dimensionality in Amazonia is due to the complex canopy tree structures found in the LiDAR vertical profiles. There is much lower dimensionality in the Stanford image caused by buildings acting as impervious surfaces to laser energy. We observe the opposite for VNIR data, which provides 64 and 37 significant PCs in the Stanford and Amazon cases, respectively. This is likely caused by the highly diverse mix of materials (e.g. chemicals) in natural and human-built surfaces found in the Stanford imagery. In contrast, Amazonian plant canopies show somewhat reduced data dimensionality

in visible and near-infrared wavelengths. This results from consistently strong absorption by photosynthetic pigments, and strong scattering associated with high leaf area index, in tropical canopies, which together dominate the VNIR wavelength range. Combining LiDAR and VNIR sensors leads to a near linear increase in data dimensionality beyond what was provided by each sensor individually (Fig. 9). This result demonstrates the orthogonal and complementary nature of the two types of measurements: LiDAR is sensitive to structure, whereas VNIR is sensitive to chemistry and composition.

After removing the water vapor regions of the original 428 contiguous channels (380–2510 nm range), the remaining 335 channels of VSWIR measurements boost the data dimensionality by 400% over that obtained when using VNIR (370–1050 nm) measurements alone (Fig. 9). The percentage increase is consistent in both the Stanford and Amazon cases. However, in the Stanford case, adding shortwave-infrared data (1100–2510 nm) provides nearly 200 additional degrees of freedom in the spectral observation suite, while the Amazon case contains about 100 additional PCs. Independent of image composition, this result highlights the value of collecting data in the shortwave-infrared range (sensu Asner & Lobell, 2000; Ceccato et al., 2001; Drake et al., 1999). Adding LiDAR observations to the VSWIR data results in a 12% increase data dimensionality in the Stanford case, and 41% in the Amazon case. Again, the boosted information content of LiDAR data in the forested scene is due to the porous, highly diverse structural composition of the rainforest canopy.

Combining all three sensor data streams into a single measurement suite yields the highest data dimensionality among the PCA analyses (Fig. 9). In the Stanford case, a 336-dimension data set is achieved. In the Amazon case, 218 dimensions are identifiable – likely the highest levels of data dimensionality reported for a forested ecosystem. The extremely high fidelity of the three-sensor data stream is expressed in PC composite images such as in Fig. 10, which shows the influence of diverse compositional and structural information embedded in the measurement suite. The Amazon case is particularly interesting because these forests are among the most biologically diverse in the world (Condit et al., 2005), yet their functional and structural variation remains largely unknown to science. The functional characteristics of forest canopies are captured in spectrometer measurements mostly by way of foliar chemistry, as well as in the amount and orientation of the leaves (Ollinger, 2011), while canopy structure is captured by LiDAR measurements sensitive to variation in canopy height, crown shape, and the vertical layering of plant tissues from the canopy top to the ground below. Our results strongly suggest that even a small landscape of 300 ha shown here contains an enormously diverse composition that has not been observed until high-fidelity, multi-sensor data fusion was applied here.

The boosted information content gleaned by integrating seemingly redundant VSWIR and VNIR data streams occurs because each instrument samples at different wavelength intervals and nominal ground sampling distances. Moreover, noise – which reduces data dimensionality – is distributed unevenly across each sensor's detector array, both spatially and spectrally, and the noise is not coherent between sensors. By acquiring combined measurements from sensors with inherent differences in spatial and spectral resolution, sampling, and noise distributions, the data dimensionality increases 5–17% when adding the VNIR to the VSWIR–LiDAR combination (Fig. 9).

## 6. Sensitivity to sensor misalignment

While there is strong scientific value in developing fully integrated, high-fidelity observations, there persists a danger of overestimating its potential if the data co-alignment is not accomplished with high precision. For example, it is common practice to compile imaging data from multiple sensors flown on separate aircraft, often with incompatible designs or settings. While average RMS errors for

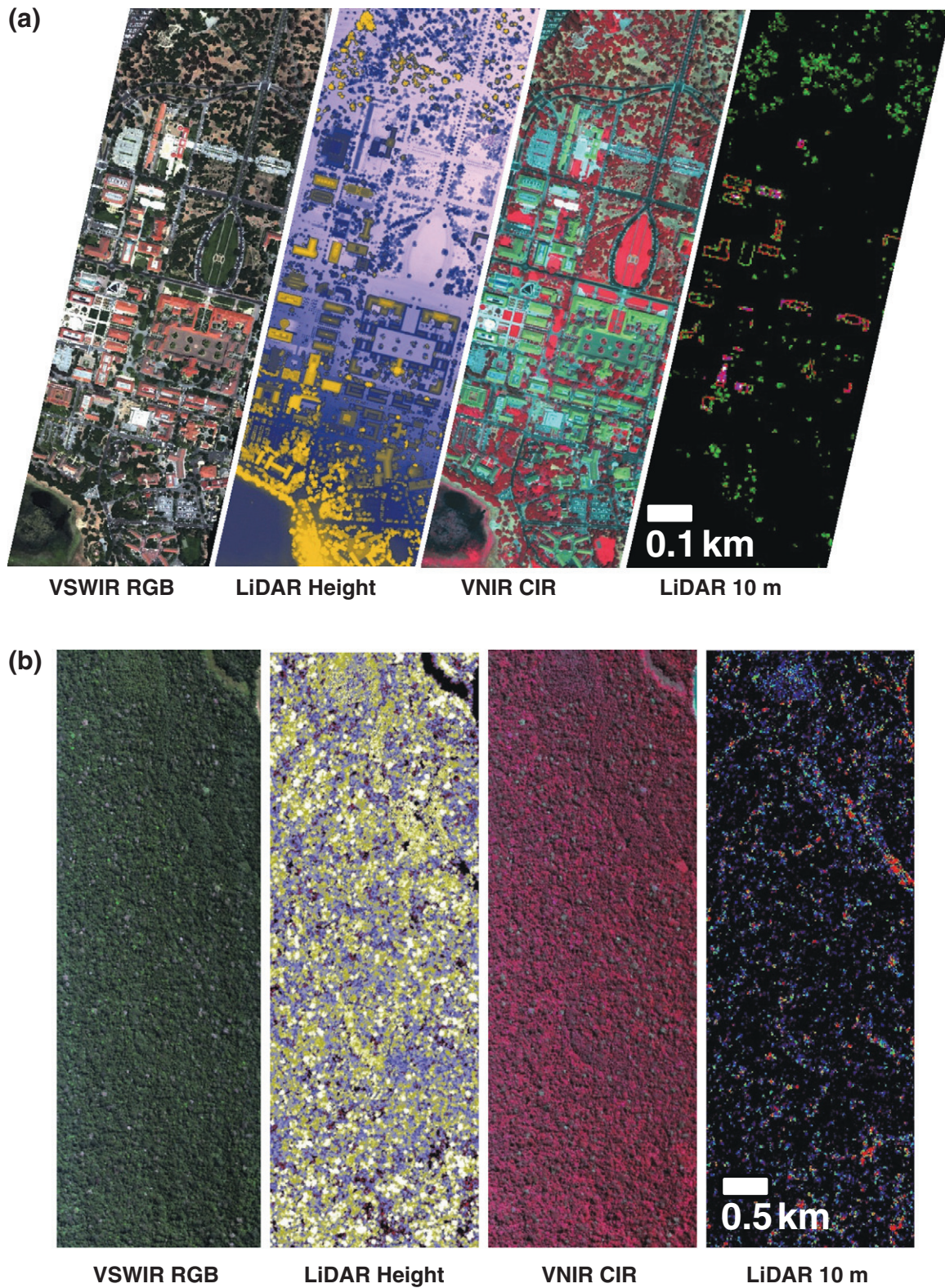


**Fig. 7.** Example CAO AToMS data sets for (a) 100 ha of Stanford University and (b) 300 ha of lowland Amazonian forest indicate the tight co-alignment of the data stream, from left to right: VSWIR true-color composite, LiDAR height above ground, VNIR color-infrared composite, and LiDAR vertical profile slice at 10 m aboveground.

data fusion are often reported to be  $\pm 1$ – $2$  pixels, this metric does not report the full range of misalignment errors that often exists within and between datasets, known as non-linear or “rubbersheet” spatial errors. Using PCA, we quantified our sensitivity to misalignment

between VSWIR, LiDAR and VNIR sensors to ascertain the extent to which data dimensionality might be reduced. We resampled each sensor data set using a separate set of GCPs to which normal random error was introduced with a mean of zero and standard deviation of

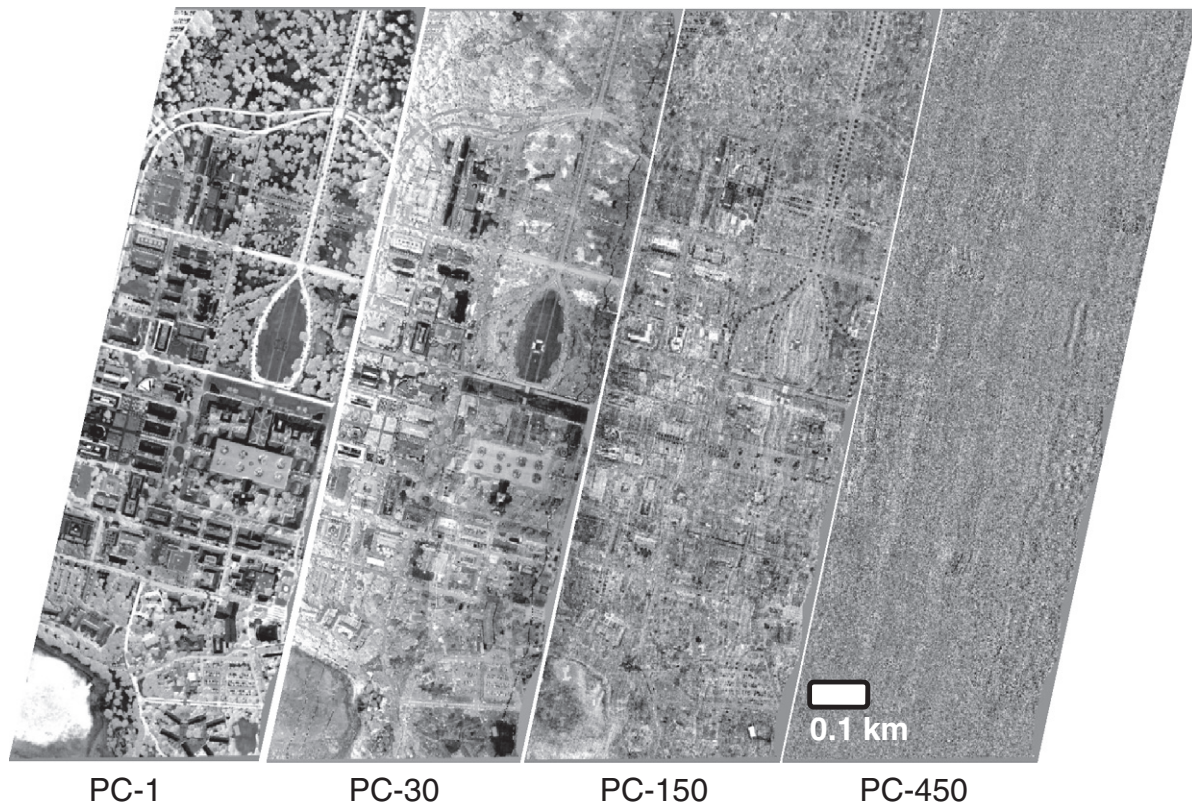


**Fig. 8.** Principal component (PC) bands of a PC analysis conducted on the full three-sensor CAO AToMS instrument suite over Stanford University. Notice the high dimensionality of the data, expressed in the clearly visible objects (buildings, vegetation, etc.) in PCs 1, 30 and 150. Noise dominates in PC band 450, for comparison.

3.0 in order to approximate an RMS of 3 pixels in both the X and Y directions. A different set of random errors was generated to produce a different misalignment for each data set (VSWIR, VNIR, and LiDAR).

The results show that even small misalignments degrade the data dimensionality (Fig. 11). In the Amazon case, misalignment between VNIR and LiDAR, or between VSWIR and LiDAR, reduces the information by 30–48%. Errors in the Stanford case are lower – 7% to 24% depending upon sensor combination – because the objects in the scene such as buildings, roads and parking lots are much larger than

the tree crowns found in the Amazon. Analyses of co-aligned imagery containing large, homogeneous features are less prone to noise introduced by inter-sensor misalignments. Some of the negative impact is also diminished here by use of the full three-sensor AToMS configuration simply by increasing the likelihood that two out of three instruments, each providing many degrees of analytical freedom, are aligned in any given portion of the field of view. Note that this is a very conservative test; data misalignments can be expressed in more insidious forms, such as when non-random misalignments occur from errors in navigation data streams or camera models.

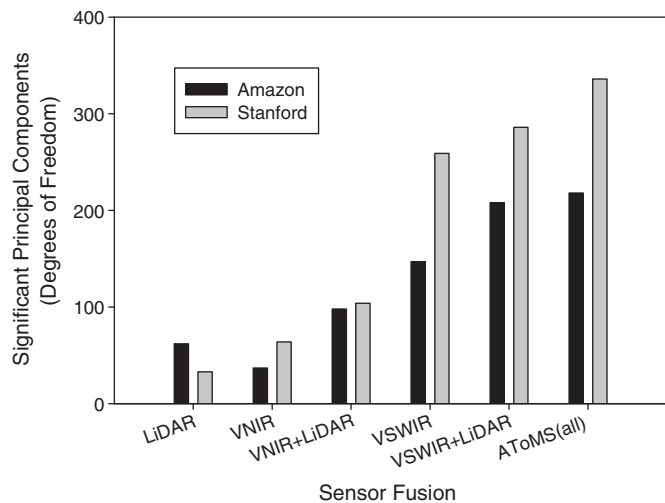


**Fig. 9.** The number of spatially significant principal components (PC), or degrees of freedom, in CAO AToMS imagery collected over Stanford University and lowland Amazonian forest (see Fig. 7). Repeated PC analysis was done on precisely co-aligned LiDAR, VNIR, and VSWIR data, as well as combinations of data from these three sensor subsystems.

## 7. Conclusions

As the scientific community pushes to understand changes in the composition of our biosphere, there is increasing demand for large-scale, spatially detailed observations that simultaneously provide data on multiple ecological properties. Without such multi-dimensional observations, a change in an unobserved ecological trait (e.g., canopy architecture) could impart a change in one that is observed (e.g., photosynthetic light absorption). Yet the unique role of either trait may differentially explain an underlying control and or a relationship regulating a process of interest, such as carbon and water fluxes, or habitat and biodiversity change. The simultaneity of the observations is therefore requisite to attributing cause and effect among the potential ecological drivers of and responses to environmental change.

More broadly, the use of spatially fused and diverse physical measurements could have a very positive effect on ecological research in coming decades. Modern ecology has grappled with resolving processes at the most appropriate spatial scales; the airborne perspective and instrument payloads such as the CAO AToMS will continue to transform our measurement capabilities from localized plot to regional levels. Through these approaches, new ecological understanding is already

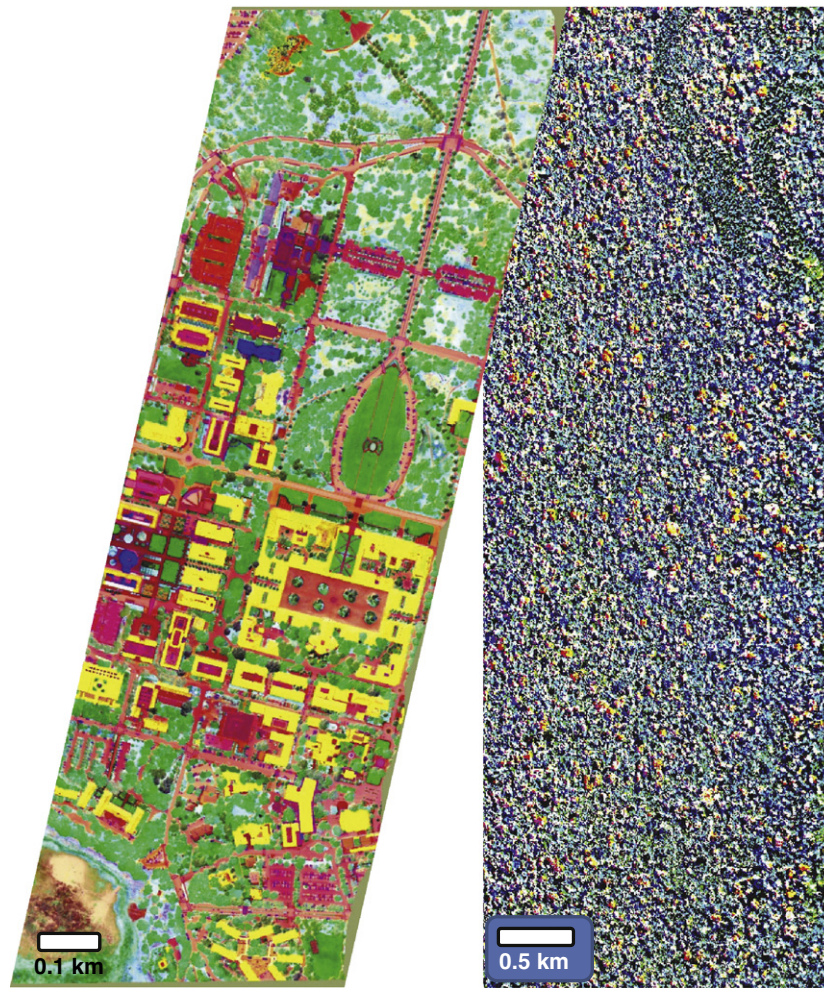


**Fig. 10.** Composite images for (a) Stanford University and (b) lowland Amazonia of principal components analysis (PCA) bands 2, 3 and 4 representing compositional and structural diversity observed with CAO ATOMS.

emerging at the macroscale, and with fine biological resolution. As a result, the observations will continue to facilitate discoveries that have eluded ecology, while also improving the conservation and policy relevance of scientific studies. One persisting challenge is that airborne measurements lack a certain multi-temporal feasibility due to cost and logistics. Aircraft cannot cover all geographies on a frequent basis,

so more work is needed to develop approaches which use satellite observations to inform the types of tactical mapping measurements provided by airborne remote sensing (Asner, 2009).

Here we have demonstrated that fully-integrated, macroscale ecological observations are technologically and scientifically possible, thereby greatly increasing the data dimensionality needed for new scientific analyses. Reports of 200 or more degrees of freedom in a single, geographically limited data set are rare. To our knowledge, this is the highest dimensionality of remotely sensed data reported in ecology. However, we also highlighted the losses incurred when the data stream suffers from misalignment (or non-uniformity) among the sensors contributing to the suite of observations. The instrumentation and methods described here provide a guide for those planning to develop and deploy fused sensor packages, as clearly the potential gains for environmental remote sensing are very large.

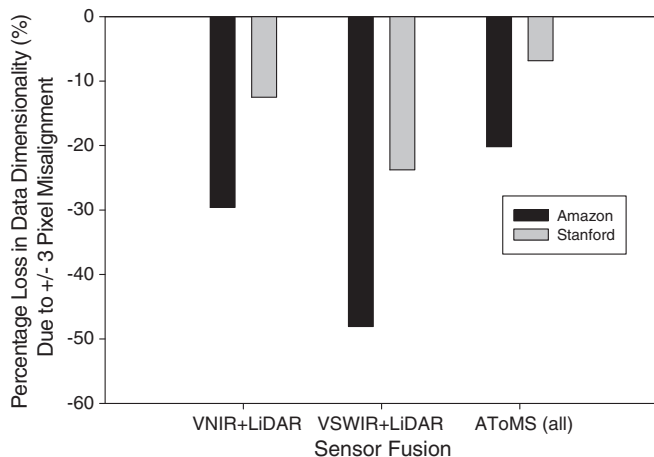


**Fig. 11.** Percentage decrease in data dimensionality or number of spatially significant principal components caused by instrument data misalignment during fusion. These errors are scene-dependent, and should not be treated as absolute values.

### Acknowledgments

The Carnegie Airborne Observatory is supported by the Gordon and Betty Moore Foundation, the John D. and Catherine T. MacArthur Foundation, the Grantham Foundation for the Protection of the Environment, the W.M. Keck Foundation, and William Hearst III.

### References

Asner, G. P. (2009). Tropical forest carbon assessment: Integrating satellite and airborne mapping approaches. *Environmental Research Letters*, 3, 1748–9326.

- Asner, G. P., Knapp, D. E., Kennedy-Bowdoin, T., Jones, M. O., Martin, R. E., Boardman, J., & Field, C. B. (2007). Carnegie Airborne Observatory: In-flight fusion of hyper-spectral imaging and waveform light detection and ranging (LiDAR) for three-dimensional studies of ecosystems. *Journal of Applied Remote Sensing*, 1. <http://dx.doi.org/10.1117/1111.2794018>.
- Asner, G. P., Knapp, D. E., Kennedy-Bowdoin, T., Jones, M. O., Martin, R. E., Boardman, J., & Hughes, R. F. (2008). Invasive species detection in Hawaiian rainforests using airborne imaging spectroscopy and LiDAR. *Remote Sensing of Environment*, 112, 1942–1955.
- Asner, G. P., Loarie, S. R., & Heyder, U. (2010). Combined effects of climate and land-use change on the future of humid tropical forests. *Conservation Letters*, 3, 395–403.
- Asner, G. P., & Lobell, D. B. (2000). A biogeophysical approach for automated SWIR unmixing of soils and vegetation. *Remote Sensing of Environment*, 74, 99–112.
- Asner, G. P., Martin, R. E., Knapp, D. E., Tupayachi, R., Anderson, C., Carranza, L., Martinez, P., Houcheime, M., Sinca, F., & Weiss, P. (2011). Spectroscopy of canopy chemicals in humid tropical forests. *Remote Sensing of Environment*, 115, 3587–3598.
- Babey, S. K., & Anger, C. D. (1989). A compact airborne imaging spectrographic imager (CASI). *IGARSS '89: 12th Canadian Symposium on Remote Sensing*, 2. (pp. 1028–1031).
- Bay, H., Andreas, E., Tuytelaars, T., & Van Gool, L. (2008). Speeded-up robust features (SURF). *Computer Vision and Image Understanding*, 10, 346–359.
- Biggs, R., Carpenter, S. R., & Brock, W. A. (2009). Turning back from the brink: Detecting an impending regime shift in time to avert it. *Proceedings of the National Academy of Sciences*, 106, 826–831.
- Blackburn, G. A. (2002). Remote sensing of forest pigments using airborne imaging spectrometer and LiDAR imagery. *Remote Sensing of Environment*, 82, 311–321.
- Boelman, N. T., Asner, G. P., Hart, P. J., & Martin, R. E. (2007). Multi-trophic invasion resistance in Hawaii: Bioacoustics, field surveys, and airborne remote sensing. *Ecological Applications*, 17, 2137–2144.
- Bohlman, S. (2008). Hyperspectral remote sensing of exposed wood and deciduous trees in seasonal tropical forests. In M. Kalacska, & G. A. Sanchez-Azofeifa (Eds.), *Hyperspectral remote sensing of tropical and subtropical forests* (pp. 177–192). Boca Raton, FL: CRC Press.
- Bonan, G. B., Levis, S., Kergoat, L., & Oleson, K. W. (2002). Landscapes as patches of plant functional types: An integrating concept for climate and ecosystem models. *Global Biogeochemical Cycles*, 16, 101029–101059.
- Ceccato, P., Flasse, S., Tarantola, S., Jacquemoud, S., & Gregoire, J. M. (2001). Detecting vegetation leaf water content using reflectance in the optical domain. *Remote Sensing of Environment*, 77, 22–33.
- Clark, M. L., Clark, D. B., & Roberts, D. A. (2004). Small-footprint LiDAR estimation of sub-canopy elevation and tree height in a tropical rain forest landscape. *Remote Sensing of Environment*, 91, 68–89.
- Clark, M. L., Roberts, D. A., & Clark, D. B. (2005). Hyperspectral discrimination of tropical rain forest tree species at leaf to crown scales. *Remote Sensing of Environment*, 96, 375–398.
- Clark, M. L., Roberts, D. A., Ewel, J. J., & Clark, D. B. (2011). Estimation of tropical rain forest aboveground biomass with small-footprint LiDAR and hyperspectral sensors. *Remote Sensing of Environment*, 115, 2931–2942.
- Clark, R. N., Swayze, G. A., Livo, K. E., Kokaly, R. F., Sutley, S. J., Dalton, J. B., McDougal, R. R., & Gent, C. A. (2003). Imaging spectroscopy: Earth and planetary remote sensing with the USGS Tetracorder and expert systems. *Journal of Geophysical Research*, 108, 1–44.
- Coles, J. B., Richardson, B. S., Eastwood, M. L., Sarture, C. M., Quetin, G. R., Hernandez, M. A., Kroll, L. A., Nolte, S. H., Porter, M. D., & Green, R. O. (2011). Spectrally and radiometrically stable wide-band on-board calibration source for in-flight data validation in imaging spectroscopy applications. *2011 IEEE Aerospace Conference*. Big Sky, MT USA: IEEE.
- Condit, R., Ashton, P., Balslev, H., Brokaw, N., Bunyavejchewin, S., Chuyong, G., Co, L., Dattaraja, H. S., Davies, S., Esufali, S., Ewango, C. E. N., Foster, R., Gunatilleke, N., Gunatilleke, S., Hernandez, C., Hubbell, S., John, R., Kenfack, D., Kiratiprayoon, S., Hall, P., Hart, T., Itoh, A., LaFrankie, J. V., Liengola, I., Lagunzad, D., De Lao, S. L., Losos, E., Magard, E., Makana, J., Manokaran, N., Navarrete, H., Nur, S. M., Okhubo, T., Perez, R., Samper, C., Seng, L. H., Sukumar, R., Svenning, J. -C., Tan, S., Thomas, D., Thompson, J., Vallejo, M. I., Munoz, G. V., Valencia, R., Yamakura, T., & Zimmerman, J. K. (2005). Tropical tree alpha-diversity: Results from a worldwide network of large plots. *Science*, 308, 565–582.
- Dalponte, M., Bruzzone, L., & Gianelle, D. (2008). Fusion of hyperspectral and LiDAR remote sensing data for classification of complex forest areas. *IEEE Transactions on Geoscience and Remote Sensing*, 46, 1416–1427.
- DeFries, R. S., & Townsend, J. R. G. (1995). NDVI-derived land cover classifications at a global scale. *International Journal of Remote Sensing*, 15, 3567–3586.
- Doughty, C., Asner, G., & Martin, R. (2011). Predicting tropical plant physiology from leaf and canopy spectroscopy. *Oecologia*, 165, 289–299.
- Drake, N. A., Mackin, S., & Settle, J. J. (1999). Mapping vegetation, soils, and geology in semiarid shrublands using spectral matching and mixture modeling of SWIR AVIRIS imagery. *Remote Sensing of Environment*, 68, 12–25.
- Fensham, R. J., & Fairfax, R. J. (2002). Aerial photography for assessing vegetation change: A review of applications and the relevance of findings for Australian vegetation history. *Australian Journal of Botany*, 50, 415–429.
- Field, C. B., Behrenfeld, M. J., Randerson, J. T., & Falkowski, P. (1998). Primary production of the biosphere: Integrating terrestrial and oceanic components. *Science*, 281, 237–240.
- French, J. R. (2003). Airborne LiDAR in support of geomorphological and hydraulic modelling. *Earth Surface Processes and Landforms*, 28, 321–335.
- Gamon, J. A., Field, C. B., & Ustin, S. L. (1992). Evaluation of spatial productivity patterns in an annual grassland during an AVIRIS overflight. In R. O. Green (Ed.), *Third Annual JPL Airborne Geoscience Workshop* (pp. 17–19).
- Gao, B. C., Goetz, A. F. H., & Wiscombe, W. J. (1993). Cirrus cloud detection from airborne imaging spectrometer data using the 1.38  $\mu\text{m}$  water vapor band. *Geophysical Research Letters*, 20, 301–304.
- Gao, B. -C., & Goetz, A. F. H. (1990). Column atmospheric water vapor and vegetation liquid water retrievals from airborne imaging spectrometer data. *Journal of Geophysical Research*, 95, 3549–3564.
- Gitelson, A. A., & Merzlyak, M. N. (1997). Remote estimation of chlorophyll content in higher plant leaves. *International Journal of Remote Sensing*, 18, 2691–2697.
- Green, R. O. (1998). Spectral calibration requirement for Earth-looking imaging spectrometers in the solar-reflected spectrum. *Applied Optics*, 37, 683–690.
- Green, R. O., Eastwood, M. L., & Sarture, C. M. (2005). Advances in the Airborne Visible and Infrared Imaging Spectrometer (AVIRIS), 1987–2005. In R. O. Green (Ed.), *NASA Airborne Earth Science Workshop*. Pasadena, CA: Jet Propulsion Laboratory.
- Green, R. O., Eastwood, M. L., Sarture, C. M., Chrien, T. G., Aronsson, M., Chippendale, B. J., Faust, J. A., Pavri, B. E., Chovit, C. J., Solis, M. S., Olah, M. R., & Williams, O. (1998). Imaging spectroscopy and the Airborne Visible Infrared Imaging Spectrometer (AVIRIS). *Remote Sensing of Environment*, 65, 227–248.
- Green, R. O., & Pavri, B. E. (2002). AVIRIS inflight calibration experiment results for 2001. In R. O. Green (Ed.), *Proceedings of the 2002 Airborne Earth Science Workshop* (pp. 1–13). Pasadena, CA USA: Jet Propulsion Laboratory, California Institute of Technology.
- Harding, D. J., Lefsky, M. A., Parker, G. G., & Blair, J. B. (2001). Laser altimeter canopy height profiles: Methods and validation for closed-canopy, broadleaf forests. *Remote Sensing of Environment*, 76, 283–297.
- Hatfield, J. L. (1984). Intercepted photosynthetically active radiation estimated by spectral reflectance. *Remote Sensing of Environment*, 14, 65–75.
- Hill, R. A., & Thomson, A. G. (2005). Mapping woodland species composition and structure using airborne spectral and LiDAR data. *International Journal of Remote Sensing*, 26, 3763–3779.
- Kalacska, M., Bohlman, S., Sanchez-Azofeifa, G. A., Castro-Esau, K., & Caelli, T. (2007). Hyperspectral discrimination of tropical dry forest lianas and trees: Comparative data reduction approaches at the leaf and canopy levels. *Remote Sensing of Environment*, 109, 406–415.
- Kampe, T. U., Johnson, B. R., Kuester, M., & McCorkel, J. (2011). Airborne remote sensing instrumentation for NEON: Status and development. *IEEE (Ed.), Aerospace Conference*. Big Sky, MT.
- Knox, N. M., Skidmore, A. K., Prins, H. H. T., Asner, G. P., van der Werff, H. M. A., de Boer, W. F., van der Waal, C., de Knegt, H. J., Kohi, E. M., Slotow, R., & Grant, R. C. (2011). Dry season mapping of savanna forage quality, using the hyperspectral Carnegie Airborne Observatory sensor. *Remote Sensing of Environment*, 115, 1478–1488.
- Kokaly, R. F., Asner, G. P., Ollinger, S. V., Martin, M. E., & Wessman, C. A. (2009). Characterizing canopy biochemistry from imaging spectroscopy and its application to ecosystem studies. *Remote Sensing of Environment*, 113, S78–S91.
- Lee, A. C., & Lucas, R. M. (2007). A LiDAR-derived canopy density model for tree stem and crown mapping in Australian forests. *Remote Sensing of Environment*, 111, 493–518.
- Lefsky, M. A., Cohen, W. B., Parker, G. G., & Harding, D. J. (2002). LiDAR remote sensing for ecosystem studies. *BioScience*, 52, 19–30.
- Loarie, S. R., Duffy, P. B., Hamilton, H., Asner, G. P., Field, C. B., & Ackerly, D. D. (2009). The velocity of climate change. *Nature*, 462, 1052–1057.
- Martin, M. E., Plourde, L. C., Ollinger, S. V., Smith, M. -L., & McNeil, B. E. (2008). A generalizable method for remote sensing of canopy nitrogen across a wide range of forest ecosystems. *Remote Sensing of Environment*, 112, 3511–3519.
- Mascaro, J., Asner, G. P., Muller-Landau, H. C., van Breugel, M., Hall, J., & Dahlin, K. (2011). Controls over aboveground forest carbon density on Barro Colorado Island, Panama. *Biogeosciences*, 8, 1615–1629.
- McGraw, J. B., Warner, T. A., Key, T. L., & Lamar, W. R. (1998). High spatial resolution remote sensing of forest trees. *Tree*, 13, 301–302.
- Medvigy, D., & Moorcroft, P. R. (2012). Predicting ecosystem dynamics at regional scales: An evaluation of a terrestrial biosphere model for the forests of northeastern North America. *Philosophical Transactions of the Royal Society B*, 367, 222–235.
- Medvigy, D., Wofsy, S. C., Munger, J. W., Hollinger, D. Y., & Moorcroft, P. R. (2009). Mechanistic scaling of ecosystem function and dynamics in space and time: Ecosystem demography model version 2. *Journal of Geophysical Research*, 114, G01002.
- Mouroulis, P., & Green, R. O. (2003). Optical design for high-fidelity imaging spectrometry. *Proceedings of SPIE The International Society for Optical Engineering*, 4829(II), 1048.
- Mouroulis, P., Green, R. O., & Chrien, T. G. (2000). Design of pushbroom imaging spectrometers for optimum recovery of spectroscopic and spatial information. *Applied Optics*, 39, 2210.
- Müller, J., & Brandt, R. (2009). Assessing biodiversity by remote sensing in mountainous terrain: The potential of LiDAR to predict forest beetle assemblages. *Journal of Applied Ecology*, 46, 897–905.
- Mundt, J., Streutker, D., & Glenn, N. (2006). Mapping sagebrush distribution using fusion of hyperspectral and LiDAR classifications. *Photogrammetric Engineering and Remote Sensing*, 72, 47.
- Ollinger, S. V. (2011). Sources of variability in canopy reflectance and the convergent properties of plants. *New Phytologist*, 189, 375–394.
- Parmesan, C. (2006). Ecological and evolutionary responses to recent climate change. *Annual Review of Ecology, Evolution, and Systematics*, 37, 637–669.
- Phillips, O. L., Aragao, L. E. O. C., Lewis, S. L., Fisher, J. B., Lloyd, J., Lopez-Gonzalez, G., Malhi, Y., Monteagudo, A., Peacock, J., Quesada, C. A., van der Heijden, G., Almeida, S., Amaral, I., Arroyo, L., Aymard, G., Baker, T. R., Banki, O., Blanc, L., Bonal, D., Brando, P., Chave, J., de Oliveira, A. C. A., Cardozo, N. D., Czimczik, C. I., Feldpausch, T. R., Freitas, M. A., Gloor, E., Higuchi, N., Jimenez, E., Lloyd, G., Meir, P., Mendoza, C., Morel, A., Neill, D. A., Nepstad, D., Patino, S., Penuela, M. C., Prieto, A., Ramirez, F., Schwarz, M., Silva, J., Silveira, M., Thomas, A. S., ter Steege,

- H., Stropp, J., Vasquez, R., Zelazowski, P., Davila, E. A., Andelman, S., Andrade, A., Chao, K. J., Erwin, T., Di Fiore, A., Honorio, E., Keeling, H., Killeen, T. J., Laurance, W. F., Cruz, A. P., Pitman, N. C. A., Vargas, P. N., Ramirez-Angulo, H., Rudas, A., Salamao, R., Silva, N., Terborgh, J., & Torres-Lezama, A. (2009). Drought sensitivity of the Amazon rainforest. *Science*, 323, 1344–1347.
- Porter, J., Arzberger, P., Braun, H. -W., Bryant, P., Gage, S., Hansen, T., Hanson, P., Lin, C. -C., Lin, F. -P., Kratz, T., Michener, W., Shapiro, S., & Williams, T. (2005). Wireless sensor networks for ecology. *BioScience*, 55, 561–572.
- Prieto-Blanco, X., Montero-Orille, C., Couce, B., & de la Fuente, R. (2006). Analytical design of an Offner imaging spectrometer. *Optics Express*, 14, 9156–9168.
- Ratnasingham, S., & Hebert, P. D. N. (2007). BOLD: The Barcode of Life Data System. (<http://www.barcodinglife.org>). *Molecular Ecology Notes*, 7, 355–364.
- Reinersman, P. N., & Carder, K. L. (1995). Monte-Carlo simulation of the atmospheric point-spread function with an application to correction for the adjacency effect. *Applied Optics*, 34, 4453–4471.
- Roberts, D. A., Gardner, M., Church, R., Ustin, S., Scheer, G., & Green, R. O. (1998). Mapping chaparral in the Santa Monica Mountains using multiple endmember spectral mixture models. *Remote Sensing of Environment*, 65, 267–279.
- Roberts, D. A., Green, R. O., & Adams, J. B. (1997). Temporal and spatial patterns in vegetation and atmospheric properties from AVIRIS. *Remote Sensing of Environment*, 62, 223–240.
- Schlaepfer, D., Borel, C. C., & Keller, J. (1996). *Atmospheric pre-corrected differential absorption techniques to retrieve columnar water vapor: Application to AVIRIS 91/95 data*.
- Sellers, P. J. (1985). Canopy reflectance, photosynthesis and transpiration. *International Journal of Remote Sensing*, 6, 1335–1372.
- Somers, B., Asner, G. P., Tits, L., & Coppin, P. (2011). Endmember variability in spectral mixture analysis: A review. *Remote Sensing of Environment*, 115, 1603–1616.
- Swayze, G. A., Smith, K. S., Clark, R. N., Sutley, S. J., Pearson, R. M., Vance, J. S., Hageman, P. L., Briggs, P. H., Meier, A. L., Singleton, M. J., & Roth, S. (2000). Using imaging spectroscopy to map acidic mine waste. *Environmental Science & Technology*, 34, 47–54.
- Thomas, V., Finch, D. A., McCaughey, J. H., Noland, T., Rich, L., & Treitz, P. (2006). Spatial modelling of the fraction of photosynthetically active radiation absorbed by a boreal mixedwood forest using a LiDAR–hyperspectral approach. *Agricultural and Forest Meteorology*, 140, 287–307.
- Turner, W., Spector, S., Gardiner, N., Fladelland, M., Sterling, E., & Steininger, M. (2003). Remote sensing for biodiversity and conservation. *Trends in Ecology & Evolution*, 18, 306–314.
- Ustin, S. L., & Gamon, J. A. (2010). Remote sensing of plant functional types. *New Phytologist*, 186, 795–816.
- Ustin, S. L., Gitelson, A. A., Jacquemoud, S., Schaepman, M., Asner, G. P., Gamon, J. A., & Zarco-Tejada, P. (2009). Retrieval of foliar information about plant pigment systems from high resolution spectroscopy. *Remote Sensing of Environment*, 113, S67–S77.
- Ustin, S. L., Roberts, D. A., Gamon, J. A., Asner, G. P., & Green, R. O. (2004). Using imaging spectroscopy to study ecosystem processes and properties. *BioScience*, 54, 523–534.
- Varga, T. A., & Asner, G. P. (2008). Hyperspectral and LiDAR remote sensing of fire fuels in Hawaii Volcanoes National Park. *Ecological Applications*, 18, 613–623.
- Verma, S. B., Sellers, P. J., Walthall, C. L., Hall, F. G., Kim, J., & Gowtz, S. J. (1993). Photosynthesis and stomatal conductance related to reflectance on the canopy scale. *Remote Sensing of Environment*, 44, 103–116.
- Wake, D. B., Hadly, E. A., & Ackerly, D. D. (2009). Biogeography, changing climates and niche evolution. *Proceedings of the National Academy of Sciences*, 106, 19631–19637.